

SOURCE PROCESS AND GROUND MOTIONS OF THE 2008 WENCHUAN EARTHQUAKE*

K. Koketsu¹, Y. Yokota², H. Ghasemi³, K. Hikima³, H. Miyake⁴, and Z. Wang⁵

¹ Professor, Earthquake Research Institute, University of Tokyo, Japan (koketsu@eri.u-tokyo.ac.jp)

² Graduate Student, School of Science, University of Tokyo, Japan

³ Postdoctoral Fellow, Earthquake Research Institute, University of Tokyo, Japan

⁴ Assistant Professor, Earthquake Research Institute, University of Tokyo, Japan

⁵ Professor, Institute of Engineering Mechanics, China Earthquake Administration, China

ABSTRACT: We studied the source process of the Wenchuan earthquake using not only teleseismic waveforms observed by FDSN/IRIS but also strong motion waveforms observed by the Institute of Engineering Mechanics of the China Earthquake Administration. We first defined a two-segment source fault according to surface rupture investigations and the aftershock distribution by the United States Geological Survey. The southern and northern segments were given similar strikes, but different dip angles based on the results of point sources analyses. We next carried out a finite source inversion of the teleseismic waveform data. The result of this inversion indicates M_w 7.9, the maximum slip of about 9 m, and two asperities in the southern and northern segments. The southern asperity is much stronger than the northern one. Mostly reverse faulting occurred up to 60km from the hypocenter, but strike slips are dominant beyond 60km. Significant slips appear in a 250 km long region (10,000 km²) of the source fault. These length and area are close to the averages for M_w 7.9 low-angle reverse-faulting earthquakes. We then performed a joint inversion of both the teleseismic and strong motion data. The result of the joint inversion still keeps similar features to those found in the result of the inversion of the teleseismic data only. We can also find some discrepancies such as strike-slip components in the southern asperity and shallow slips in the southern segment. The detailed structures of the asperities are shown in the result of the joint inversion. The strong motion records closest to the source fault mainly consist of the ground motions from the southern asperity and the slips around the hypocenter. They overlap each other because of the rupture velocity nearly equal to the S-wave velocity, resulting in strong directivity effects at the end of the southern segment. Heavily damaged towns such as Yingxiu and Beichuan and the zones of seismic intensity XI were located just above the southern asperity or at the end of the southern segment.

Key Words: Wenchuan earthquake, source process, teleseismic data, strong motion data, asperity, directivity effect

* Parts of this report were taken from a paper submitted to "International Conference on Earthquake Engineering for the 1st Anniversary of Wenchuan Earthquake."

INTRODUCTION

The 2008 Wenchuan earthquake of M_w (moment magnitude) 7.9 occurred in eastern Sichuan, China at 6:28UT on May 12, 2008, causing 69,226 fatalities, 17,923 missing and 374,643 injuries (as of September 18, 2008). The economic losses have reached 845,100,000,000 yuan. To estimate the source process of this earthquake, we observed the locations of surface ruptures and determined the source fault. We then inverted teleseismic records in the world and a few strong ground motion records in the source region. We next compared the resultant slip distribution to the distributions of aftershocks, geological structures, seismic intensities, and peak ground accelerations.

SURFACE RUPTURES AND AFTERSHOCK DISTRIBUTION

The Longmen Shan thrust belt consists of three fault zones (Wenchuan-Maowen, Yingxiu-Beichuan, and Guanxian-Anxian). Since surface ruptures often appear on the ground surface for a crustal earthquake such as the 2008 Wenchuan earthquake, we can estimate the location of its source fault from the locations of these surface ruptures. Surface ruptures were observed by Japanese societies reconnaissance teams and Hao et al. (2008a, b). Another was found in ALOS PRISM images by Koarai et al. (2008) (Fig. 1).

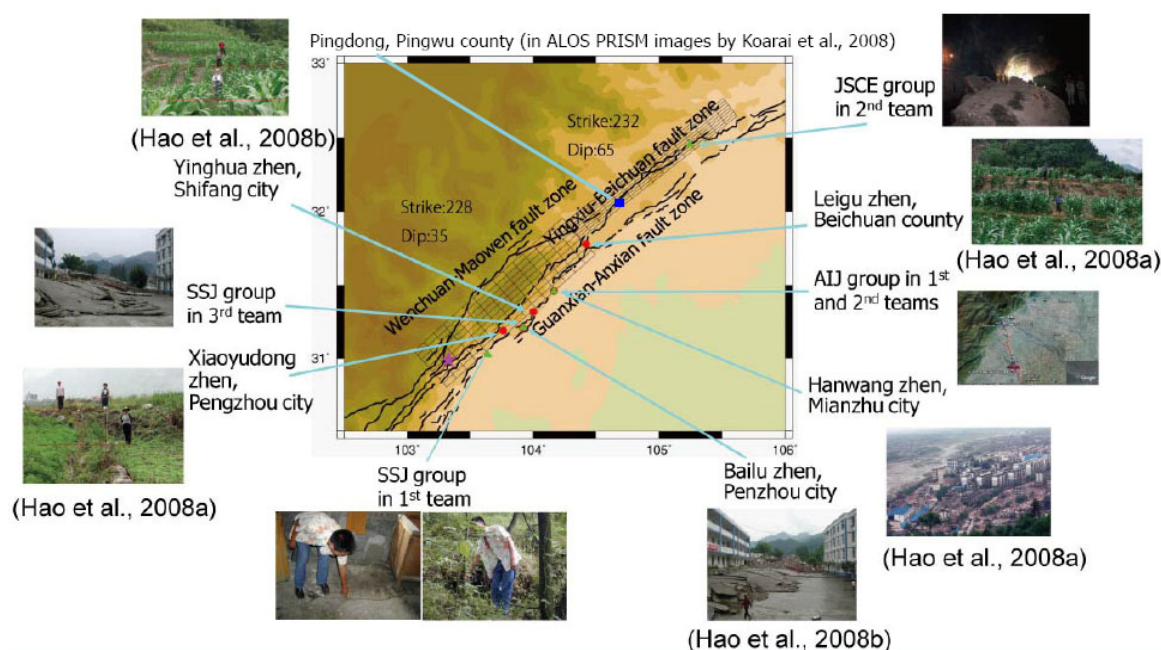


Fig. 1 Locations of surface ruptures observed by the Japanese societies reconnaissance teams and Hao et al. (2008a, b), and Koarai et al. (2008). Black lines denote active fault traces identified by Kirby et al. (2003), Burchfiel et al. (1995), and Densmore et al. (2007). The meshed rectangles represent the source fault model.

We also examined the distribution of aftershocks determined by USGS (Fig. 2) and the result of point sources analyses by the method of Kikuchi and Kanamori (1991) (Fig. 3). Based on these observations and analyses, we then constructed the source fault model shown in Figures 1 and 2 such that the upper sides of the fault rectangles are aligned along the lines connecting the sites of surface ruptures.

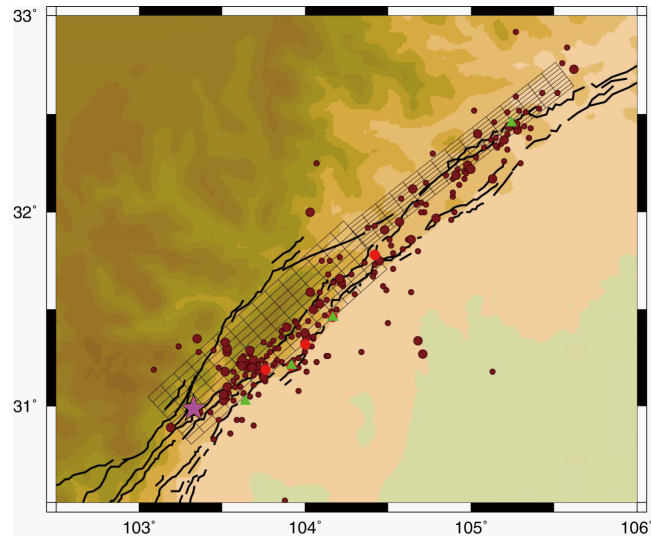


Fig. 2 Distribution of aftershocks (brown circles) and the hypocenter (pink star) determined by USGS. The surface ruptures and active fault traces overlie or underlie them. The meshed rectangles represent the source fault model.

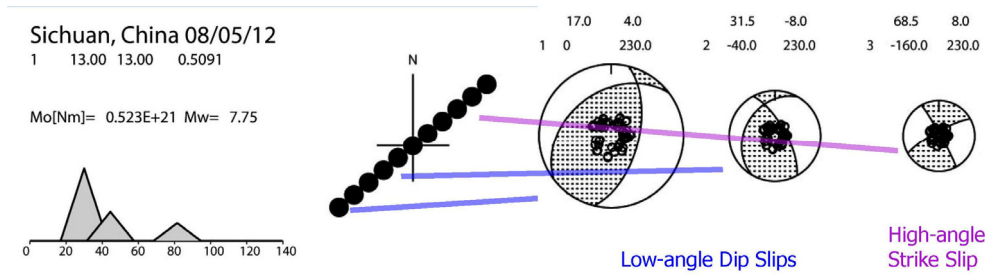


Fig. 3 Results of the point sources analyses by the method of Kikuchi and Kanamori (1991). Two point sources were obtained in the southern part with low-angle dip slips, while the third point source was located in the northern part with a high-angle strike slip.

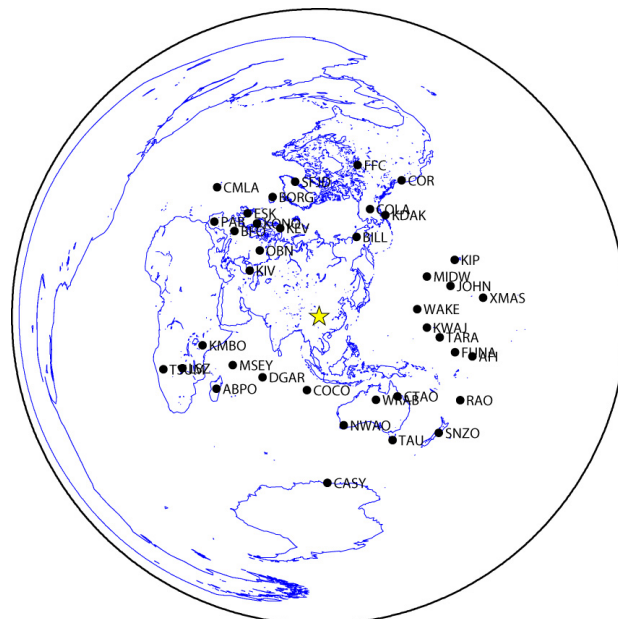


Fig. 4 Stations observing the teleseismic waveforms used in the inversions.

INVERSION OF TELESEISMIC DATA

We then carried out a finite source inversion of the first 140 s of the teleseismic waveforms (Fig. 4) using the Green's functions of Kikuchi and Kanamori (1991) and the inverse algorithm of Yoshida et al. (1996) with modifications by Hikima and Koketsu (2005). We also used the location of the hypocenter determined by USGS as a rupture initiation point.

The inversion achieved the agreement shown in Figure 5. Its results indicate a seismic moment of 1.0×10^{21} Nm (M_w 7.9) and the maximum slip of about 9 m. In the resultant slip distribution (Fig. 6), significant slips occurred in an area of $250 \times 40 = 10,000$ km² (this is about an average; Fig. 7). There are mostly reverse faulting slips up to 60 km from the hypocenter, while there are mostly strike slips beyond 60 km. There is one asperity on each half. The southern asperity is much stronger and larger than the northern one. These asperities look surrounded by the aftershocks, as shown in Fig. 8.

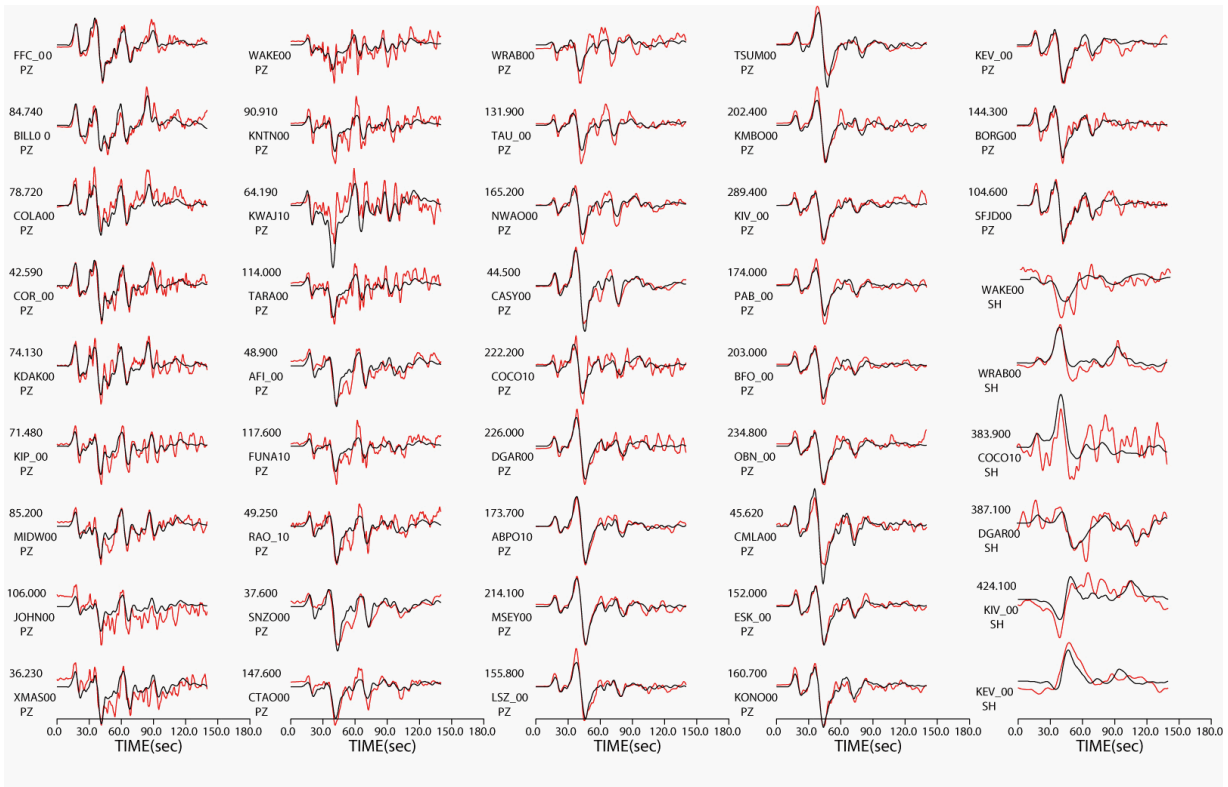


Fig. 5 Comparison of observed and synthetic waveforms from the inversion of teleseismic data.

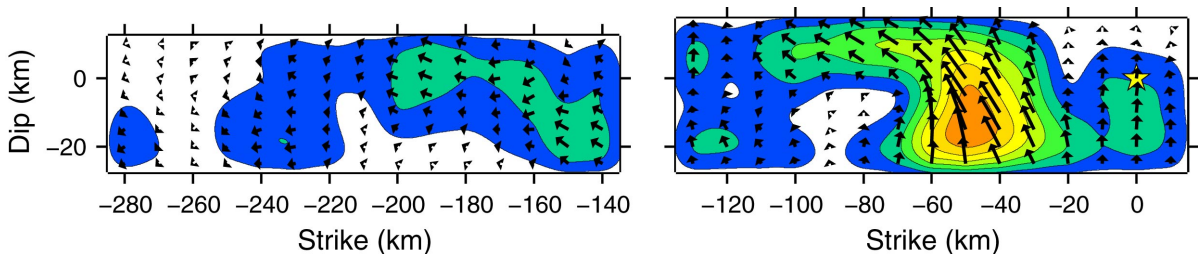


Fig. 6 Resultant slip distribution by the source inversion of the teleseismic waveforms.

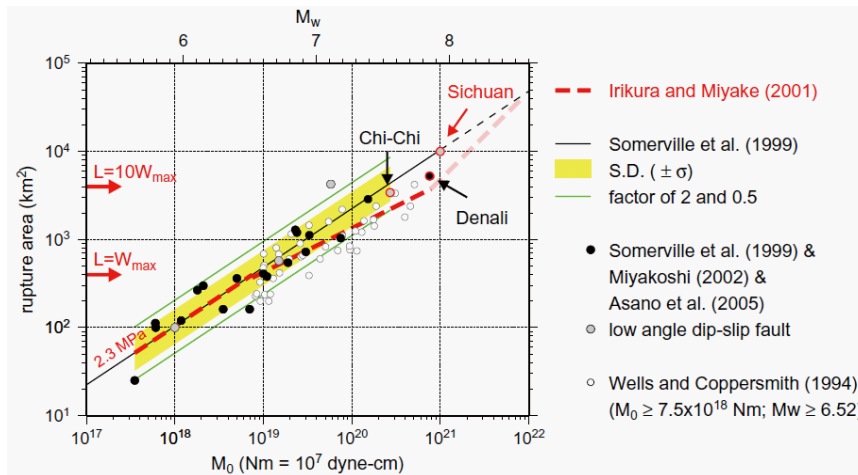


Fig. 7 Scaling of rupture areas with respect to seismic moment.

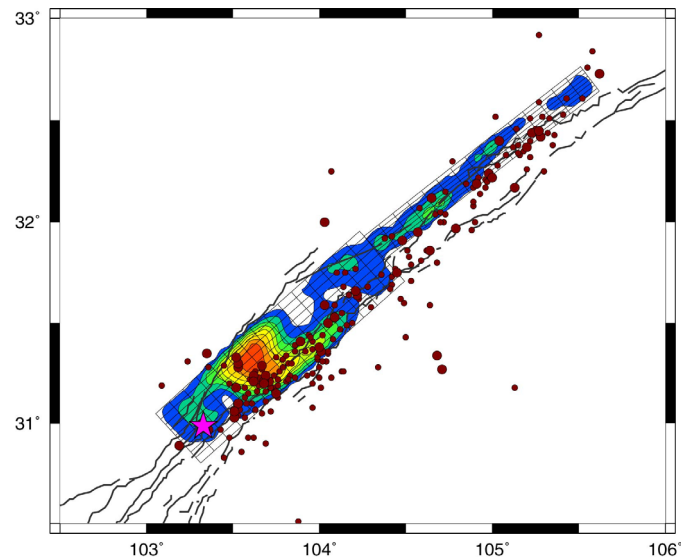


Fig. 8 Projection of the slip distribution onto the ground surface and the distribution of aftershocks.

JOINT INVERSION OF TELESEISMIC AND STRONG MOTION DATA

We next introduced the strong motion records observed at six stations close to the source region (Fig. 9). These data were published in Supplement of Vol. 28 of *Journal of Earthquake Engineering and Engineering Vibration* in October of 2008. We performed a joint inversion of them and the teleseismic data used in the previous section. The Green's functions were calculated by the extended reflectivity method of Kohketsu (1985).

The slip distribution (movements on the northwestern hanging wall) obtained by this joint inversion is shown in Fig. 10. Fig. 11 shows its projection onto the ground surface, associated with the aftershocks and active fault traces. The comparison of Figs. 10 and 11 with Figs. 6 and 8 for the inversion of strong motion records only suggests the detailed structures of the asperities such as the shape of the southern asperity, though the seismic moment and M_w are almost unchanged. We can also find some discrepancies such as strike-slip components in the southern asperity and shallow slips in the southern segment.

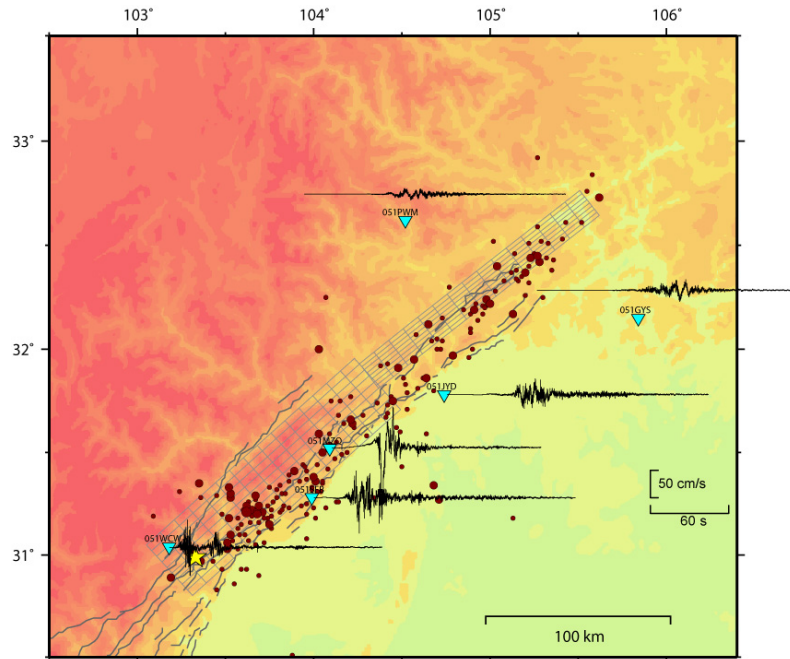


Fig. 9 E-W components of the strong motion records observed at the six stations close to the source region (turquoise triangles). The yellow star denotes the rupture initiation point (hypocenter).

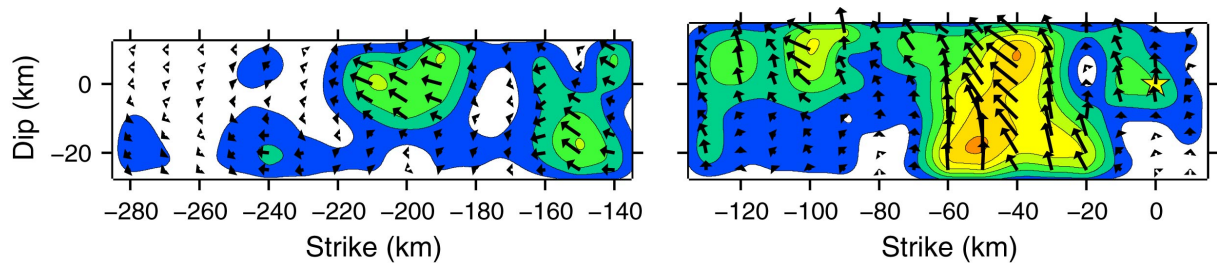


Fig. 10 Resultant slip distribution by the joint inversion of the teleseismic and strong motion waveforms.

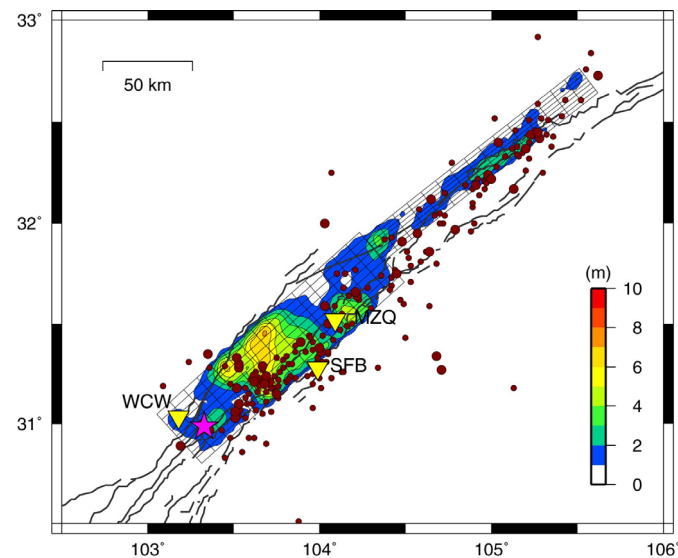


Fig. 11 Projection of the slip distribution in Fig. 10 onto the ground surface and the distribution of aftershocks.

GROUND MOTIONS

The strong motion records closest to the source fault mainly consist of the ground motions from the southern asperity and the slips around the hypocenter. They overlap each other because of the rupture velocity (V_r) nearly equal to the S-wave velocity (V_s). Heavily damaged towns such as Yingxiu and Beichuan and the zones of seismic intensity XI determined by the Institute of Engineering Mechanics (IEM; Fig. 12) were located just above the southern asperity or at the end of the southern segment. The V_r nearly equal to V_s resulted in strong directivity effects and these caused the damaging ground motion at the end of the southern segment, as shown in Fig. 13.

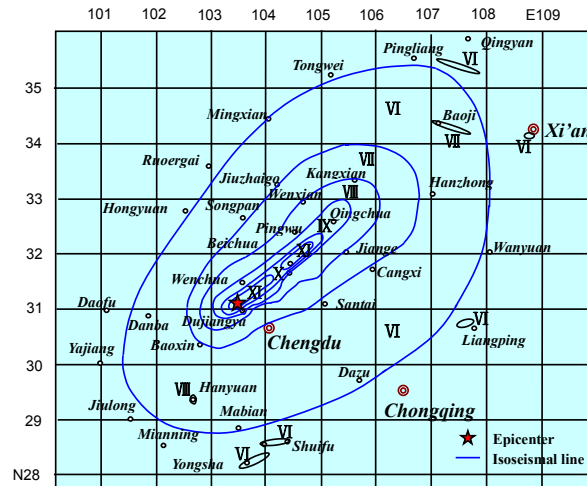


Figure 12 Distribution of seismic intensities.

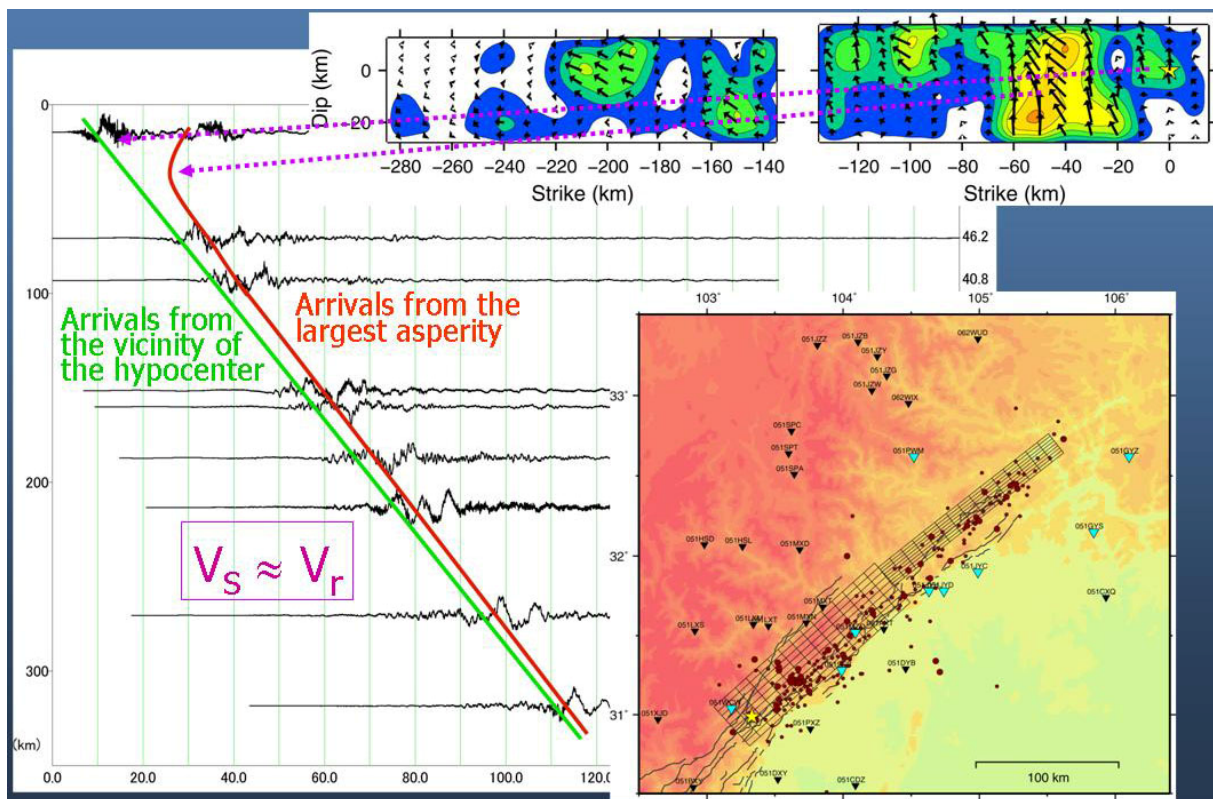


Fig. 13 Section of vertical velocity seismograms.

ATTENUATION RELATIONS

In order to study the attenuation of strong motions during the 2008 Wenchuan earthquake (M_w 7.9), we finally considered 54 triaxial accelerograms, recorded at distances shorter than 150 km. The main reason for this selection criterion is due to the fact that far-field records, due to their large source-to-site distances, are of low engineering significance (Ambraseys et al., 2005). In addition such records may perturb the data distribution because instruments far from the earthquake will only trigger for large-amplitude ground motions, and the regression results may thereby be biased (Fukushima, 1997; Fukushima and Tanaka, 1990). The distribution of selected strong motion stations is shown in Fig. 14.

A fourth-order acausal Butterworth filter is used to adjust the baseline as well as to reduce the noise in the selected accelerograms. The Peak Ground Acceleration (PGA) as well as Peak Ground Velocity (PGV) values of horizontal components are then determined from the processed accelerograms. In order to estimate the corresponding fault distance for each recording station we considered the fault-plane geometry mentioned in the previous sections. The surface projection of the considered fault-plane is shown in Fig. 14. The final functional form selected to describe the attenuation of PGA and PGV with distance is:

$$\log_{10} Y = a_1 + a_2 R - \log_{10} (R + a_3 10^{(0.42M)})$$

Where Y is the predicted PGA (cm/s^2) or PGV (cm/s), R is the fault distance in km , M is the moment magnitude of the Wenchuan event (M_w 7.9), and $a_1 - a_3$ are the regression coefficients. In the assumed model the addition of the term ($a_3 10^{(0.42M)}$) to R in the geometrical spreading term allows the amplitude saturation in the near-fault region to be expressed (Fukushima et al., 2003). The functional form adopted here requires both linear and nonlinear parameters to be determined. We take advantage of the equation's separable structure to apply an efficient, robust solution technique: accordingly, a direct search technique known as the Nelder-Mead algorithm is used to search for values of the nonlinear parameters that minimize the norm of residuals. At each step of the search process, the linear parameters are estimated via maximum likelihood estimation by maximizing the log-likelihood function over the estimation parameters (Joyner and Boore, 1993).

Fig. 15 and Fig. 16 show the comparison between predicted and observed PGA and PGV values, respectively. The scatter plots of the residuals with respect to distance for PGA and PGV are shown in the second and third rows of Fig. 15 and Fig. 16, respectively. The thick solid lines in these graphs are the best-fitting least-squares lines, calculated in order to detect any possible trends in the distribution of the residuals with respect to the explanatory variable (distance R). The model parameters for the fitted lines and their 95% confidence intervals are calculated and are not significantly different from zero at the 5% significance level and hence the null hypothesis that the residuals are dependent on

distance can be rejected at these periods. In Fig. 17 the observed PGA values as well as several curves, presenting predictions made by several attenuation models, are shown. As can be seen models developed by Kanno *et al.* (2008) and Si and Midorikawa (2004) based on Japan strong motion data, overestimate PGA while other models, namely Boore and Atkinson (2008, for California), Fukushima *et al.* (2003, for West Eurasia), and Ghasemi *et al.* (2009, for Iran) underestimate PGA at most of the distance range; However the latter models, on average, seem to be in better agreement with observed points than those developed for Japan.

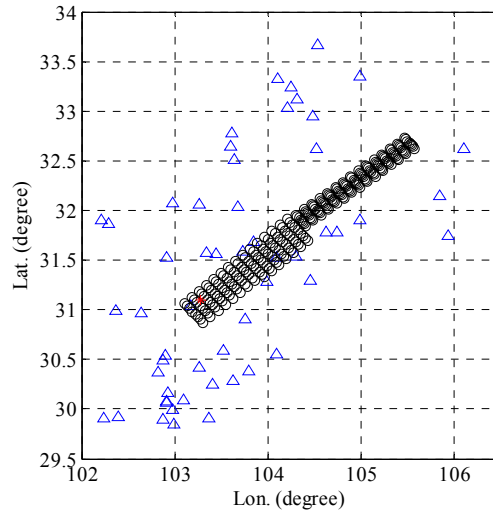


Fig. 14. Distribution of the selected recording stations and the source fault model.

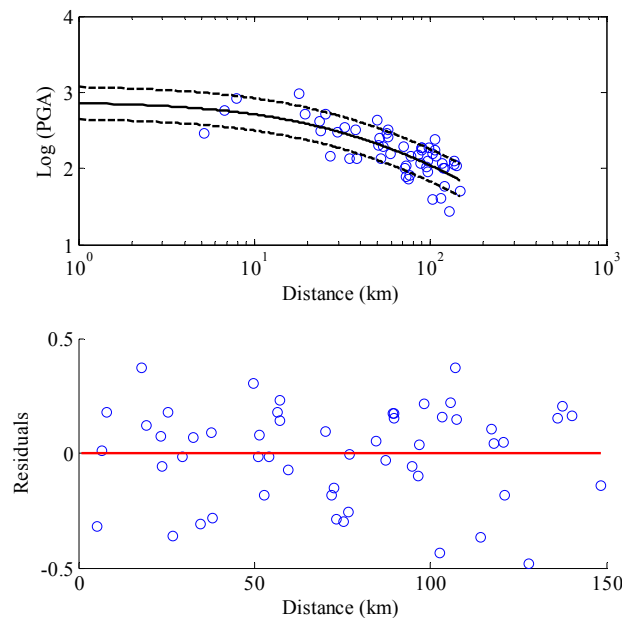


Fig. 15 Comparison between predicted PGA for the derived attenuation model and observed PGA values. The dashed lines indicate +1 and -1 standard deviations. The distribution of residuals between the observed and predicted accelerations with respect to distance is also shown.

